Volume 20 | Number 45 | 7 December 2018 | Pages 28351–28944

PCCP

Physical Chemistry Chemical Physics

rsc.li/pccp

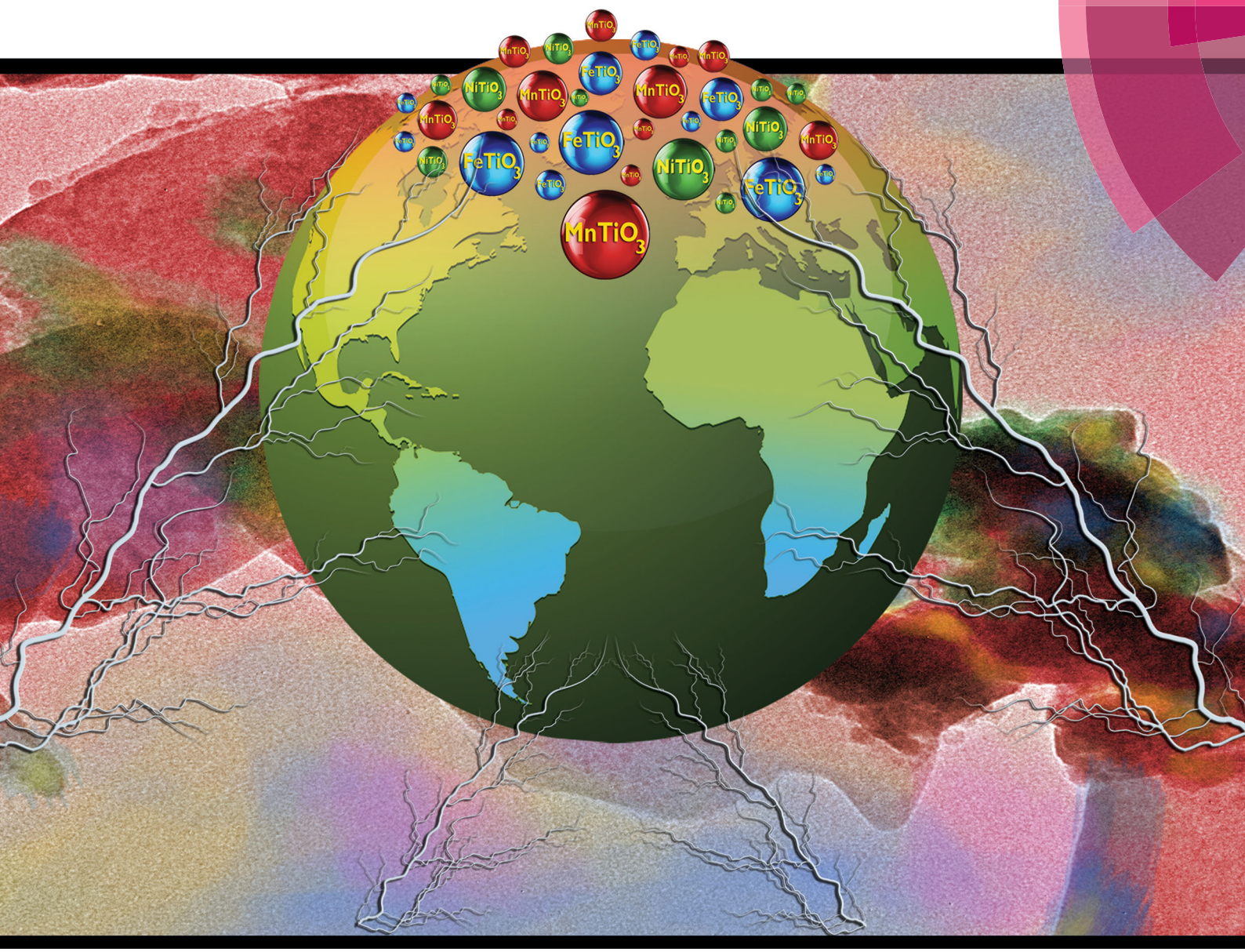

ISSN 1463-9076

ROYAL SOCIETY OF CHEMISTRY

PAPER

J. Andrés *et al.*

A DFT investigation of the role of oxygen vacancies on the structural, electronic and magnetic properties of $ATiO_3$ (A = Mn, Fe, Ni) multiferroic materials

PCCP

PAPER

View Article Online
View Journal | View Issue

Cite this: *Phys. Chem. Chem. Phys.*, 2018, **20**, 28382

A DFT investigation of the role of oxygen vacancies on the structural, electronic and magnetic properties of $ATiO_3$ (A = Mn, Fe, Ni) multiferroic materials†

R. A. P. Ribeiro, [a] E. Longo, [b] J. Andrés *[c] and S. R. de Lazaro [a]

Received 13th July 2018,
Accepted 28th August 2018

DOI: 10.1039/c8cp04443k

rsc.li/pccp

In order to achieve deep insight into the multiferroic behavior and electronic properties of intrinsic oxygen vacancies in $ATiO_3$ (A = Mn, Fe, Ni), first-principles calculations based on hybrid density functional theory were carried out for bulk and non-polar (110) surface models. We found that the formation of an oxygen vacancy is accompanied by structural and electronic disorders in the constituent clusters of $[TiO_6]$ and $[AO_6]$ in $ATiO_3$, that become $[TiO_5]$ and $[AO_5]$, respectively. This perturbation contributes to the generation of intermediary energy levels in the band gap region, thus narrowing the required excitation energy. In addition, the remaining electrons are mainly trapped in the empty 3d orbitals of the Ti cations neighboring the oxygen vacancy, generating $[TiO_5]'$ ($3d^1$) that mediates an antiferromagnetic to ferromagnetic transition in $MnTiO_3$ and $FeTiO_3$ materials. In particular, $MnTiO_3$ surfaces show exposed $[TiO_4]'$ species that are responsible for its half-metallic behavior. The present work provides compelling evidence that controlling oxygen vacancies can be a valuable strategy to tailor the multiferroic properties of $ATiO_3$ materials.

1. Introduction

Multiferroic materials are capable of combining different ferroic properties (magnetism, ferroelectricity, and elasticity) and have attracted a large amount of scientific attention due to their technological applications, mainly in the electronics industry.[1–3] In particular, ABO_3-type materials are widely investigated for technological purposes, such as ferroelectric devices, gas sensors, actuators and others, because they can display a variety of physical and chemical properties depending on the metal atoms occupying the A and B-sites.[4] Therefore, new multiferroic materials can be synthesized based on this class of compounds. For instance, ilmenite-based $ATiO_3$ (A = Mn, Fe, Co, Ni) materials have been widely studied for their intriguing magnetoelectric effects.[5–15]

In previous studies of this class of compounds, we noted that changes in both the A- and B-site cations induce structural and electronic distortions that drastically modify their magnetic and electrical behaviors, which are the main targets of multiferroic materials design.[16–18] An alternative method of inducing these distortions in solid state materials relies on the presence of oxygen vacancies (V_O). This type of defect is common in metallic oxides due to the crystal growth process, annealing, or substitutions inside the crystalline structure leading to electronic defects (excess electrons or holes) that can modify several features (structural, optical, electrical, magnetic, and others) of solid state materials.[19] Recently, theoretical and experimental studies have determined that oxygen vacancies play a fundamental role in tuning the optical, electrical, and magnetic properties of oxides.[20–26] For instance, Pacchioni *et al.* described ferromagnetism in reduced ZrO_{2-x} nanoparticles and indicated that neutral oxygen vacancies can induce local ferromagnetism in non-magnetic 4d cations through a ferromagnetic arrangement between reduced Zr^{3+} centers.[27,28] The same authors also predicted local magnetism in other materials such as WO_3, TiO_2, and NiO by using both bulk and surface models.[29,30] However, it is important to point out that the existence of reduced centers does not guarantees the existence of ferromagnetism, because the spins located at the reduced centers could be antiparallel ordered, as reported for TiO_2.[31]

It is widely recognized that ferromagnetic–ferroelectric (FEM–FE) behavior is more desirable than antiferromagnetic–ferroelectric (AFM–FE) behavior for multiferroic applications.[32,33] In this context, the presence of V_O is crucial because it can

[a] *Department of Chemistry, State University of Ponta Grossa, Av. General Carlos Cavalcanti, 4748, 84030-900, Ponta Grossa, PR, Brazil*
[b] *CDMF-UFSCar, Universidade Federal de São Carlos, PO Box 676, São Carlos 13565-905, SP, Brazil*
[c] *Department of Physical and Analytical Chemistry, University Jaume I (UJI), Castelló 12071, Spain. E-mail: andres@qfa.uji.es*

† Electronic supplementary information (ESI) available. See DOI: 10.1039/c8cp04443k

generate FEM ordering in AFM–FE materials. This fact can be ascribed to the partially disturbed (super-)exchange interactions between magnetic ions caused by bond breaking processes closer to the defect, as well as the excess charge or holes due to local non-stoichiometry altering the valence number of magnetic or non-magnetic ions near the vacancy, which leads to a change in the local magnetic moment.[34] Such a mechanism has been successfully applied to generate ferromagnetic ordering in common ferroelectric perovskite materials, such as $BaTiO_3$, $SrTiO_3$, and $PbTiO_3$, thus enabling them to exhibit magneto-electric coupling.[21,26,35–38] In addition, Li and co-authors have reported that the presence of V_O controls magnetism and ferro-electric ordering, demonstrating that oxygen vacancies create $[TiO_5]'$ ($3d^1$) defect states, mediating the ferromagnetic coupling between the localized Eu ($4f^7$) spins, and increase the off-center displacement of Ti cations, enhancing the ferroelectric order.[39,40] Similar results were found by Cheng *et al.* and Deng *et al.* for $YMnO_3$ multiferroic materials using both experimental techniques and theoretical calculations.[41,42]

Experimental and theoretical studies have been developed to elucidate the role of defects on the multiferroic properties of $BiFeO_3$, the most studied single-phase multiferroic material, which has a high ferroelectric Curie temperature (T_c = 1103 K) and antiferromagnetic Neel temperature (T_N = 643 K).[43,44] More recently, Rojac *et al.*[45] reported atomic-scale chemical and structural analyses showing that the accumulation of charged defects at domain walls in $BiFeO_3$ provided superior electrical properties for the samples, an observation that was confirmed by Schrade *et al.*[45,46] On the other hand, focusing on the defect-driven antiferromagnetic–ferromagnetic transition, Wu *et al.* noted an unusual ferromagnetism in samples synthesized with low-temperature, fast, solid-state reactions, which was attributed to the presence of oxygen-deficient centers that suppress the spin circular cycloid in $BiFeO_3$.[47] Further, several theoretical studies have confirmed such predictions, showing that oxygen vacancies affect the magnetic moments at neighboring Fe ions. These vacancies, along with additional ferroelectric polarizations due to the cation displacement, provide the rich variety of multiferroic behaviors observed in $BiFeO_3$ based on the concentration and charge of defect states.[34,48–50]

Transition metal titanates $ATiO_3$ (A = Mn, Fe, Ni), with $LiNbO_3$-type (*R*3*c*) ilmenite structure, are one of the most promising types of multiferroic materials due to their remarkable magneto-electric coupling. These compounds are structurally isomorphic to $BiFeO_3$ except that the positions of the A and B cations are exchanged.[9,51] In the past few years, scientific interest in such materials has increased due to the possibility of controlling their magnetic behavior based on antisymmetric Dzyaloshinskii–Moriya interactions.[8,9,12–14] The *R*3*c* structure consists of oxygen layers in a distorted hexagonal close-packed configuration, where the octahedral sites, *i.e.* $[AO_6]$ and $[TiO_6]$ clusters, are equally occupied by A and Ti cations, respectively. The magneto-electric properties are associated with the presence of A-site cations displaced from the central positions of the oxygen octahedral cages, *i.e.* $[AO_6]$ clusters, resulting in a spontaneous polarization along the (001) direction[51,52] summed to a G-type antiferromagnetic order along (111) planes. Despite current theoretical studies developed for $ATiO_3$ (A = Mn, Fe, Ni) materials, the role of oxygen vacancies in the intrinsic physical and chemical properties remains unclear.[8–14]

In this study, first-principles hybrid density functional theory (DFT) calculations were performed to provide a deep insight into the multiferroic nature and electronic properties of intrinsic point defects in $ATiO_3$ (A = Mn, Fe, Ni). In this article, the main goal is to show how the generation of oxygen-deficient centers perturbs the exchange-coupling constant between magnetic atoms and induces the formation of magnetic $[TiO_5]'$ ($3d^1$) species that contribute to the AFM–FE magnetic transition. These oxygen-deficient centers provide a general interpretation, at the atomic level, of the changes in the magnetic and electronic properties allowing us to elucidate the role of oxygen vacancies in the multiferroic properties of these materials.

This article is organized into three further sections. The computational methodology used in this study is described in the following section. The third section, where the results are presented and discussed, is divided into two main subsections. The first one discusses the properties of the bulk $ATiO_3$ (A = Mn, Fe, Ni) compounds. The second subsection deals with the non-polar (110) surfaces. The last section summarizes the main results of this work.

2. Computational methodology

DFT calculations were performed using the linear combination of atomic orbitals approach as implemented in the CRYSTAL14 code.[53] The A, Ti, and O atoms were described by atom centered all-electron Gaussian basis sets such as 86-411d41G, 86-411(d31)G, and 8-411G, respectively.[54–56] In all calculations, a PBE0[57] hybrid functional was adopted for the treatment of exchange and correlation due to its good agreement with the experimental values of many properties computed previously for pristine $ATiO_3$ (A = Mn, Fe, Ni) multiferroic materials.[18] The analyses of electronic properties by means of density of states, band structure profiles, and electron density distributions were carried out with the new functionalities for property evaluation available in the new version of CRYSTAL (2017).[58]

The pristine *R*3*c* unit cell was computed using a rhombohedral primitive unit cell that contains two $ATiO_3$ unit formulas (10 atoms) with A (A = Mn, Fe, Ni), Ti and O atoms located at (0, 0, *u*), (0, 0, 0) and (*x*, *y*, *z*), respectively.[8,12,14] The V_O vacancy was modeled in embedded 2 × 2 × 2 $ATiO_3$ supercells, containing 80 atoms which corresponds to a defect concentration of 2.1%, as represented in Fig. 1. In addition, we considered the creation of oxygen vacancies in non-polar (110) surfaces of $ATiO_3$ materials. This surface was previously found to be the most stable cleavage plane for $MnTiO_3$, dominating the ideal morphology.[59] In this case, a 2 × 1 supercell (80 atoms) was used considering three different vacancy configurations (V_{1-3}) due to the existence of three non-equivalent oxygen atoms along the surface plane. The first one (V_1) correspond to a superficial two-fold oxygen atom coordinated with A (A = Mn, Fe, Ni) and Ti cations, while

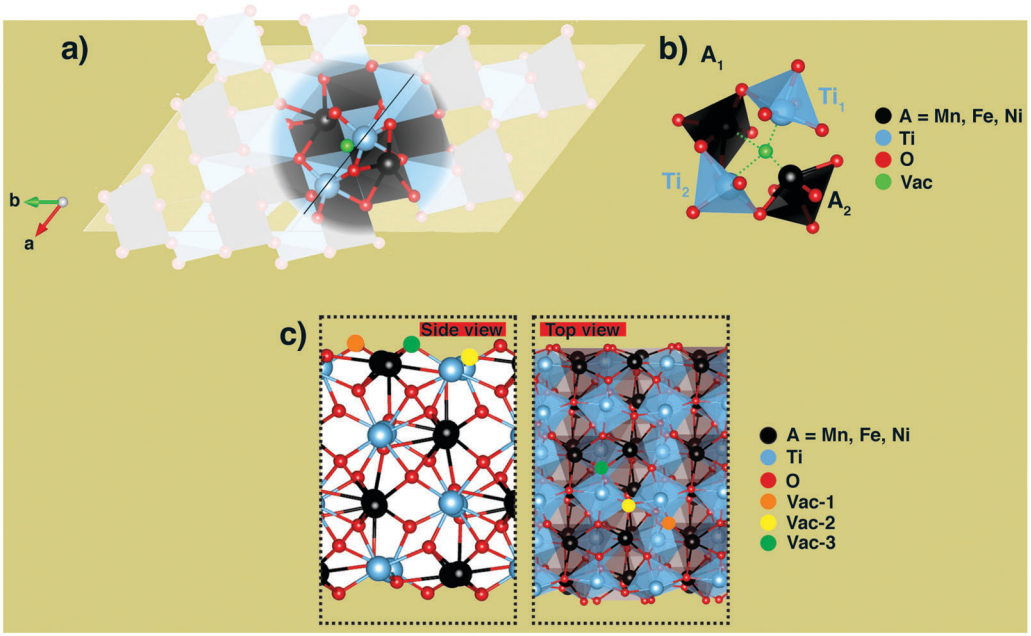

Fig. 1 (a) A schematic representation of the $ATiO_3$ (A = Mn, Fe, Ni) unit cell, where the model used to create a V_O vacancy in a $2 \times 2 \times 2$ $ATiO_3$ supercell with 80 atoms is depicted. (b) Local structure in the vicinity of V_O vacancy site and the constituent clusters are highlighted. (c) Side- and top-view for non-equivalent vacancy centers in (110) surface plane.

V_2 and V_3 correspond to a superficial three-fold oxygen atom, surrounded by two Ti and one Mn cation in the V_2 case, or coordinated with two Mn and one Ti cation in the V_3 case, as presented in Fig. 1.

Electronic integration over the Brillouin Zone was performed using an $8 \times 8 \times 8$ Monkhorst–Pack[60] *k*-mesh for the 10 atom unit cell containing 65 *k*-points. For supercell expansions, a reduced *k*-mesh density ($2 \times 2 \times 2$) was employed containing 8 *k*-points, as was performed by Bjørheim *et al.* to investigate defective $BaZrO_3$.[61] The thresholds controlling the accuracy of the Coulomb and exchange integral calculations were controlled by five thresholds set to 8, 8, 8, 8, and 16. The convergence criteria for mono- and bielectronic integrals were set to 10^{-8} Hartree, while the RMS gradient, RMS displacement, maximum gradient and maximum displacement were set to 3×10^{-5}, 1.2×10^{-4}, 4.5×10^{-5} and 1.8×10^{-4} a.u., respectively.

Following the Kroger–Vink notation,[62] the V_O can be neutral ($V_O^{\times}$), single- ($V_O^{\bullet}$), or double-positively ($V_O^{\bullet\bullet}$) charged, resulting in different mechanisms associated with the trapping of holes at the vacancy sites. Usually, the $V_O^{\times}$ originates from a diamagnetic ($\uparrow\downarrow$) center, which can be transformed into a positively charged vacancy by trapping a hole, while the remaining electron is trapped on the empty states of neighboring metal centers, resulting in a paramagnetic species ($\uparrow$). In addition, one may expect that further ionization of $V_O^{\bullet}$ sites could produce double-positively charged $V_O^{\bullet\bullet}$ centers, with null magnetic moment. However, the existence of oxygen anions (O^{2-}) requires a significant local structural relaxation in order to balance the electron density of the neighboring under-coordinated cations. In this study, only neutral $V_O^{\times}$ species were considered due to the complexity of dealing with charged supercell models in the CRYSTAL code. Here, it is important to point out that the states of a vacancy site are present due to the treatment performed with the CRYSTAL code through GHOST, where the nuclear charge is removed while the Gaussian basis sets are maintained.

Experimental results suggest a G-type antiferromagnetic ground-state for all $ATiO_3$ (A = Mn, Fe, Ni) materials consisting of spins ferromagnetically ordered within (111) planes, while the adjacent planes are antiferromagnetically coupled. In our calculations, lattice parameters and atomic positions were relaxed for both pristine and oxygen-defective models in FEM configuration. Additional single point calculations were performed to ascertain the magnetic ground-state for oxygen-defective supercells due to the remaining two electrons related to the presence of neutral $V_O^{\times}$ centers in the lattice. For this purpose, we considered two collinear magnetic configurations: (i) G-type AFM with two remaining electrons from $V_O^{\times}$ in a singlet closed-shell configuration (AFM-S); (ii) G-type AFM configuration with two remaining electrons from $V_O^{\times}$ in a triplet closed-shell configuration (AFM-T). In addition, the magnetic exchange coupling constant between the two magnetic A^{2+} cations neighboring the $V_O^{\times}$ was analyzed by means of an additional model containing the aforementioned magnetic clusters in a parallel spin orientation (FIM), keeping the remaining electrons from $V_O^{\times}$ in the previously determined ground-state (AFM-S or AFM-T).

3. Results and discussion

3.1. Bulk

Firstly, the local structural and electronic disorders originating from the presence of oxygen vacancies in $ATiO_3$ (A = Mn, Fe, Ni)

Table 1 Calculated structural parameters for both pristine and oxygen deficient $ATiO_3$ (A = Mn, Fe, Ni) materials. The lattice parameters (*a*, *b*, *c*) and M–O bond distances (M = Ti, Mn) are in Å, V in Å^3 and lattice angles (α, β, γ) are in degrees. The values 1×, 2× and 3× correspond to the bond multiplicity

Structural parameters	$MnTiO_3$	$MnTiO_3$-$V_O^{\times}$	$FeTiO_3$	$FeTiO_3$-$V_O^{\times}$	$NiTiO_3$	$NiTiO_3$-$V_O^{\times}$
a	5.448	5.454	5.427	5.499	5.417	5.419
b		5.442		5.444		
c		5.446		5.436		
V	106.698	106.553	104.465	104.174	100.474	100.474
α	57.091	57.122	56.729	56.363	55.426	55.428
β		57.049		56.269		
γ		57.024		56.173		
Ti(1)–O	1.874 (3×)	1.871 (2×)	1.866 (3×)	1.853 (1×)	1.857 (3×)	1.870 (1×)
	2.091 (3×)	2.066 (1×)	2.111 (3×)	1.868 (1×)	2.119 (3×)	1.874 (1×)
		2.070 (1×)		2.060 (2×)		2.055 (1×)
		2.113 (1×)		2.112 (1×)		2.113 (1×)
						2.144 (1×)
Ti(2)–O		1.858 (1×)		1.840 (1×)		1.823 (1×)
		1.872 (2×)		1.865 (1×)		1.856 (1×)
		2.060 (1×)		1.899 (1×)		1.857 (1×)
		2.099 (1×)		2.097 (1×)		2.069 (1×)
				2.108 (1×)		2.088 (1×)
A(1)–O	2.115 (3×)	2.094 (1×)	2.087 (3×)	2.049 (1×)	2.041 (3×)	2.027 (1×)
	2.297 (3×)	2.114 (1×)	2.196 (3×)	2.063 (1×)	2.102 (3×)	2.038 (1×)
		2.150 (1×)		2.124 (1×)		2.070 (1×)
		2.248 (1×)		2.189 (1×)		2.084 (1×)
		2.253 (1×)		2.341 (1×)		2.171 (1×)
A(2)–O		2.141 (1×)		2.069 (1×)		2.035 (1×)
		2.142 (1×)		2.131 (1×)		2.048 (1×)
		2.235 (1×)		2.162 (1×)		2.057 (1×)
		2.297 (1×)		2.166 (1×)		2.097 (1×)
		2.431 (1×)		2.375 (1×)		2.160 (1×)

materials were investigated by comparing the structural parameters (unit cell lattice parameters, atom displacement and bond distances for the clusters centered on both A and Ti cations) for pristine and defective transition metal titanates, as summarized in Table 1. The rhombohedral setting was used due to the supercell expansion of the primitive unit cell for oxygen defective systems.

An analysis of the results presented in the Table 1 clearly indicates that oxygen vacancies cause singular effects in the crystalline structure of $ATiO_3$ materials. In general, the creation of oxygen vacancies induces a small volume contraction accompanied by slight distortion of the unit cell, as defective $MnTiO_3$ and FeTiO3 models exhibit a lower symmetry ($a \neq b \neq c$ and $\alpha \neq \beta \neq \gamma$) than pristine ones. Additionally, a small distortion was detected for both metal centered clusters closer to the oxygen vacancy that arises from cationic and anionic displacements outward and toward$V_O^{\times}$, respectively. This relaxation leads to the formation of two different $[TiO_5]$ and $[MnO_5]$ clusters, changing the local symmetries from prismatic D_{3h} $[MO_6]$ clusters in the pristine unit cell to distorted square pyramidal $[MO_5]$ units in the defective model, following the equations:

$$ATiO_{3-x}^{\times} + V_O^{\times} \rightarrow ATiO_3$$

$$[AO_6] + [TiO_6] \rightarrow [AO_5 \cdots V_O] + [TiO_5 \cdots V_O] + V_O^{\times}$$

In addition, the creation of oxygen vacancies leads to a new electron density distribution along the metal centered clusters due to the perturbation of the repulsive and attractive forces acting on the A–O and Ti–O chemical bonds. Moreover, this structural distortion can generate intermediary energy levels in the electronic structures of $ATiO_3$ systems; this is a fundamental key to tuning the magnetic, ferroelectric, and electronic properties of such materials.

Aiming to describe the electron density redistribution in the vicinity of the oxygen vacancy, Hirshfeld-I analysis was performed. This kind of analysis has shown very good results for different classes of materials in comparison to Bader's analysis (QTAIM), but at a significantly lower computational cost.[58]

In Table 2 the values of the Hirshfeld-I charges and spin densities of both Ti and A centers are reported for both pristine and oxygen deficient $ATiO_3$. An analysis of the results shows that neutral oxygen vacancies induce a decrease in the positive charge on the metal neighbors and a new electron density distribution of the remaining two electrons, which become delocalized along the $[MO_5]$ and $[TiO_5]$ clusters. Indeed, it was observed that defective $MnTiO_3$ and $FeTiO_3$ exhibit a higher charge reduction for Ti cations in comparison to A cations (A = Mn, Fe), whereas defective $NiTiO_3$ behaves in an opposite way (larger reduction for Ni atoms than for Ti). Therefore, it is possible to argue that $[NiO_5]$ clusters favor electron density redistribution along the Ni–O–Ni framework to a large extent compared to $[MnO_5]$ and $[FeO_5]$, where the remaining electron density is mainly concentrated in the Ti–O–Ti moiety. These results are supported by the QTAIM analysis performed in our previous work for pristine

Table 2 Metal charges and spin populations (in parenthesis) obtained from Hirshfeld-I analysis for both pristine and oxygen deficient $ATiO_3$ (A = Mn, Fe, Ni) materials

Metals	$MnTiO_3$	$MnTiO_3$-$V_O^\times$	$FeTiO_3$	$FeTiO_3$-$V_O^\times$	$NiTiO_3$	$NiTiO_3$-$V_O^\times$
A_1	1.92 (4.46)	1.81 (4.41)	1.93 (3.60)	1.71 (3.54)	1.91 (1.70)	1.66 (1.49)
A_2		1.70 (4.49)		1.70 (3.63)		1.62 (−1.47)
Ti_1	2.55 (0.0)	2.28 (−0.13)	2.54 (0.0)	2.22 (0.12)	2.55 (0.0)	2.37 (0.04)
Ti_2		2.05 (0.36)		2.06 (0.28)		2.12 (−0.13)

$ATiO_3$ (A = Mn, Fe, Ni), where a higher covalent character for A–O bonds was observed when moving from Mn to Ni due to the increased bond critical path (BCP) electron density, derived from the extended 3d–2p overlap, mainly for the Ni–O bond.[18]

Therefore, using the electronic parameters evaluated by means of Hirshfeld analysis we can describe the electron localization in the vicinity of the vacancy using the Kroger–Vink notation for defect equations. This method is helpful to clarify the nature of electron–hole localization in the constituent clusters inside the crystalline structure, providing an atomic level point of view of the fundamental mechanism associated with electron excitation and localization which are responsible for many phenomena, such as photoluminescence and photocatalysis.[63–66] In this formalism, the charge accumulation mechanism could be described as follows using the neutral $[MO_n]^x$, positively charged $[Mo_nV_O^\bullet]^\bullet$, and negatively charged $[MO_n]'$ cluster notation:

$$[AO_5]^\times + [TiO_5]^\times + V_O^\times \rightarrow [AO_5 \cdots V_O^\bullet]^\bullet + [TiO_5 \cdots V_O]'$$

$$[AO_5 \cdots V_O^\bullet]^\bullet + [TiO_5]^\times \rightarrow [AO_5 \cdots V_O^{\bullet\bullet}] + [TiO_5 \cdots V_O]'$$

Therefore, the results presented in Table 2 suggest the existence of a reduced Ti species $[TiO_5]'$ with non-zero magnetic moment resulting from electron trapping, as has also been observed for other defective Ti-based materials.[21,26,38,39,67,68] In this context, we argue that the magnetic properties of $ATiO_3$ materials can be changed by defects due to an electron resonance between $V_O^\times$ that becomes $V_O^\bullet$ and $V_O^{\bullet\bullet}$, resulting in electron trapping at the empty 3d energy levels of Ti. This mechanism corresponds to an alternative and innovative point of view based on atomic-level simulations used to describe the nature of magnetic properties associated with the presence of vacancies.

In order to evaluate the effect of oxygen vacancies on the local and global magnetic ordering of $ATiO_3$ (A = Mn, Fe, Ni) compounds, different arrangements of spin-density alignment were considered. First of all, it was observed that all regular magnetic clusters $[AO_6]$ (A = Mn, Fe, Ni) maintain the G-type antiferromagnetic ordering observed for the pristine bulk material.[18] In addition, in all cases it was observed that the singlet configuration is the most stable arrangement of the remaining two electrons ($V_O^\times$). However, the local spin arrangement in the vicinity of the $V_O^\times$ center shows a distinct ordering moving from Mn to Ni.

For $MnTiO_3$, the obtained results indicate that FIM ordering is 9.8 meV lower in energy than the G-type AFM model. For $FeTiO_3$ as well, a relative energy difference of around 6.7 meV was observed in comparison to the AFM model. In this case, the magnetic moments of the A_1 and A_2 atoms (A = Mn, Fe) are aligned parallel to each other and the rest of Mn atoms remain in an antiparallel arrangement. On the other hand, the calculated energies for $NiTiO_3$ indicate a stable G-type AFM ordering, as for the pristine bulk material.[18] The plotted magnetization density depicted in Fig. 2 highlights the magnetic ground state near the vacancy, confirming the spin population presented in Table 1. For $MnTiO_3$ and $FeTiO_3$ the spins of the A^{2+} neighbors are parallel containing a spin-up $[TiO_5]'$ species mediating the coupling; whereas for $NiTiO_3$, Ni(1) and Ni(2) are antiparallel with a small amount of spin density at the Ti(2) center.

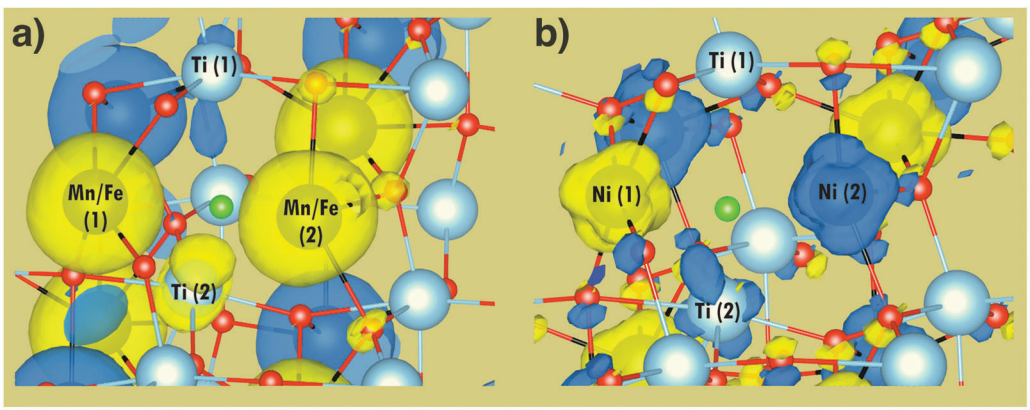

Fig. 2 Spin density distribution closer to the oxygen vacancy site showing ferromagnetic ordering for $MnTiO_3$ and $FeTiO_3$ (a) and antiferromagnetic ground state for $NiTiO_3$ (b). Yellow and blue isosurfaces correspond to the spin-up and spin-down populations, respectively. In both cases the surface isovalue is 0.01 electron $bohr^{-3}$.

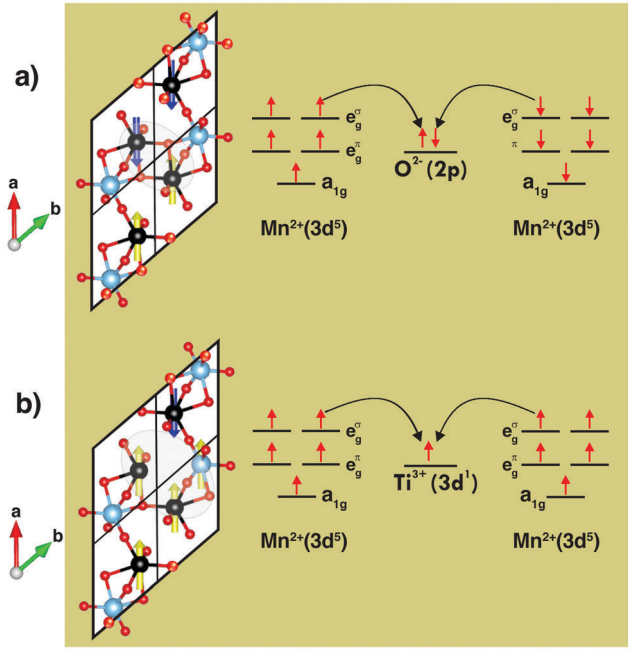

Fig. 3 A schematic representation disclosing the nature of antiferromagnetic and ferromagnetic coupling constant in pristine (a) and defective (b) $MnTiO_3$ material. The electron transfer process mediated by oxygen and Ti^{3+} atomic states is presented in the right panel confirming the spin-orientation depicted in the left panel. A similar scheme can be sketched at the $Fe^{2+}(3d^6)$ cation.

Fig. 3 presents a schematic representation of the effects of the presence of $V_O^\times$ on the experimental G-type magnetic ordering observed for $MnTiO_3$ and $FeTiO_3$ materials. Based on the analysis of the crystalline molecular orbitals, in the pristine bulk, the A–O–A antiferromagnetic exchange coupling constant derives from the extended 3d–2p overlap that enables virtual electron transfer between magnetic centers, *i.e.*, the mixing between transition metal 3d and oxygen 2p orbitals.[69] Both the direct exchange coupling constant between occupied 3d orbitals and the super-exchange coupling between A ($3d^n$) spin *via* $[TiO_5]'$ in the intermetallic A–O–Ti–O–A connection are responsible for the distinct spin arrangement neighboring the $V_O^\times$.

Let us now deeply discuss the effect of oxygen vacancies on the electronic properties of $ATiO_3$ (A = Mn, Fe, Ni) materials. For this purpose, atom/orbital resolved density of states (DOS) and band structure profiles for defective models were considered, as presented in Fig. 4a–c. In addition, the theoretical results obtained for the pristine bulk materials are presented in ESI† (Fig. S1–S3) for comparative purposes.

For $MnTiO_3$ (Fig. 4a), it was observed that $V_O^\times$ induces the creation of intermediary energy levels in the band gap region of the pristine crystalline structure (Fig. S1, ESI†), narrowing the band gap from 4.48 to 2.12 eV. In addition, the nature of excitation changes from direct (Γ–Γ) in the pristine material to indirect (FB–Γ) in $MnTiO_{3-x}$, suggesting that despite the lower band gap energy, electron–hole pair separation requires the coupling of phonons. Regarding the composition of both the valence band (VB) and the conduction band (CB), it was noted that the lower energy region of the VB is mainly composed of Mn(3d) orbitals overlapped with O(2p) states, while in the vicinity of the Fermi energy level the Ti(3d) atomic orbitals are predominant. On the other hand, the CB is composed primarily of empty states of Ti with fewer Mn(3d) and O(2p) states. Here, it is important to point out that the states of the vacancy site are present due to the treatment performed with the CRYSTAL code through GHOST, where the nuclear charge is removed while the Gaussian basis sets are maintained. Therefore, we can argue that the remaining electrons from $V_O^\times$ are trapped in the $3d_{z^2}$, $3d_{yz}$ and $3d_{x^2-y^2}$ orbitals of Ti, reducing the $[TiO_5]$ cluster to $[TiO_5]'$, which helps to stabilize the ferromagnetic order.

$FeTiO_3$ shows a similar pattern to $MnTiO_3$ regarding the distribution of atomic states, where midgap states are created from $V_O^\times$, reducing the band gap from 3.30 to 2.20 eV, which is indirect between FB and Γ *k*-points (see Fig. 4b). The major differences are ascribed to the electron trapping mechanism that involves both Fe(3d) and Ti(3d) orbitals. This fact can be confirmed by the larger energy difference between the localized energy levels generated from the vacancy (−0.8 eV and −0.1 eV). In comparison to $Mn^{2+}(3d^5)$, the orbital occupation for Fe^{2+} is different due to the pairing of electrons in the non-degenerate a_{1g} orbital that increases the crystal field splitting energy in comparison to the half-filled orbitals, which becomes higher in energy (Fig. 4b and Fig. S2, ESI†). Then, such levels are closer in energy to the intermediary levels, enabling the trapping of electrons in these orbitals, thus reducing the magnetic moment from electron-pairing, as confirmed in Table 2 which shows that the spin populations of Fe^{2+} are more affected by $V_O^\times$ than those of Mn^{2+}, once the orbital occupation is increased and the local charge changes. However, in the upper part of the VB, occupied $Ti(3d^1)$ species that contribute to the overall magnetism were observed.

On the other hand, the antiferromagnetic order of defective $NiTiO_3$ was confirmed by band structure and DOS analysis (see Fig. 4c). Similar to the other investigated materials, a reduced indirect band gap of 2.43 eV (L–Γ) was found, as compared to defect-free $NiTiO_3$ (5.12 eV). Combining the values for the spin populations reported in Table 2 and Fig. 4, it is possible to argue that the remaining electrons from $V_O^\times$ are mainly trapped in empty 3d states of Ni^{2+}, reducing the local charge, with only a few located in Ti(3d) states. In addition, the populated Ti(3d) states are closer in energy to the up- and down-spin populations, besides the similar contribution indicating an additional antiferromagnetic order between these states. In this case, we can suggest that the G-type AFM order of defective $NiTiO_3$ is stabilized by a direct exchange coupling constant between half-filled Ni(3d) orbitals that is negative due to the Pauli principle.

3.2. Non-polar (110) surfaces

The existence of oxygen defects at $ATiO_3$ (A = Mn, Fe, Ni) surfaces plays a fundamental role in its multiferroic properties, especially in the non-polar (110) surface plane which dominates

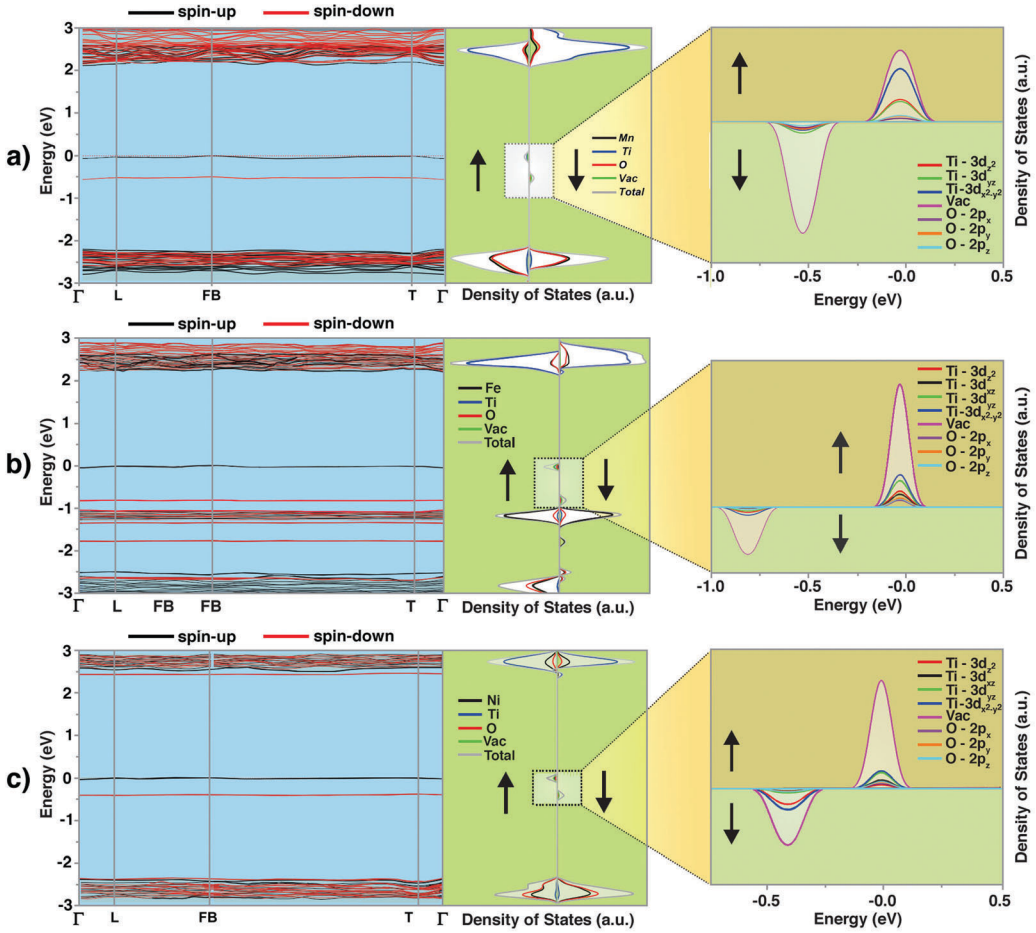

Fig. 4 Band structure profile (left panel) and atom/orbital resolved dos for (a) $MnTiO_3$, (b) $FeTiO_3$ and (c) $NiTiO_3$ materials. The inset in atom resolved dos (middle panel) is expanded with orbital compositions (right panel). The Fermi level was set as zero in all cases.

the predicted morphology for $MnTiO_3$ as it exhibits the lowest surface energy. This surface plane exhibits three symmetry-inequivalent surface oxygen atoms with distinct environments. In this case, all configurations have been calculated and the defect energies are shown in Table 3.

It is worth noting that surface coordination is important to the energetics of oxygen vacancy formation. The (110) surface plane exhibits five-fold Mn and Ti atoms, but oxygen atoms in two-fold (V_1) and three-fold centers (V_2 and V_3). In all cases, it was observed that two-fold oxygen atoms are more easily removed from the surface, due to the reduced covalent bond number. Regarding the investigated transition metal series titanates, it was noted that the defect energy is reduced from Mn to Ni in $ATiO_3$, with the lowest formation energy found for $NiTiO_3$ surfaces. This fact can be attributed to the covalent character associated with A–O bonds in this surface plane. Indeed, the removal of a bridging two-fold oxygen atom is favored for $NiTiO_3$ because the remaining Ni–O chemical bonds can counterbalance the electron density distribution along the undercoordinated Ni and Ti atoms, in a way similar to the mechanism described above which increases the local charges in bulk defective $NiTiO_3$ (Table 2).

In order to ascertain the ground-state configuration of the remaining two electrons from $V_O^\times$ centers, singlet and triplet configurations were analyzed. In this case it is important to point out that local changes in the antiferromagnetic ordering of $ATiO_3$ surfaces were not considered because the $V_O^\times$ center does not affect any A–O–A exchange coupling. For $MnTiO_3$, the remaining electrons prefer a parallel orientation, which is 8.4 meV lower in energy than the singlet. In $FeTiO_3$ as well, there is a relative energy difference of around 13.0 meV in comparison to the singlet. For $NiTiO_3$ a closed shell solution was found to be the most stable configuration for a $V_O^\times$ center. Therefore, the creation of a $V_O^\times$ center in the non-polar (110) surfaces of multiferroic $ATiO_3$ materials can generate local

Table 3 Defect formation energy (eV) for $ATiO_3$ (A = Mn, Fe, Ni) non-polar (110) surfaces. Relative energies (meV) between singlet (S) and triplet (T) multiplicities are presented for all materials considering the most stable vacancy model. The indication in parenthesis correspond to the magnetic ground-state

Models	$MnTiO_3$	$FeTiO_3$	$NiTiO_3$
V_1	5.276	4.092	3.709
V_2	5.289	4.914	4.341
V_3	5.635	5.059	4.803
Relative energy	8.39 (T)	13.17 (T)	−37.38 (S)

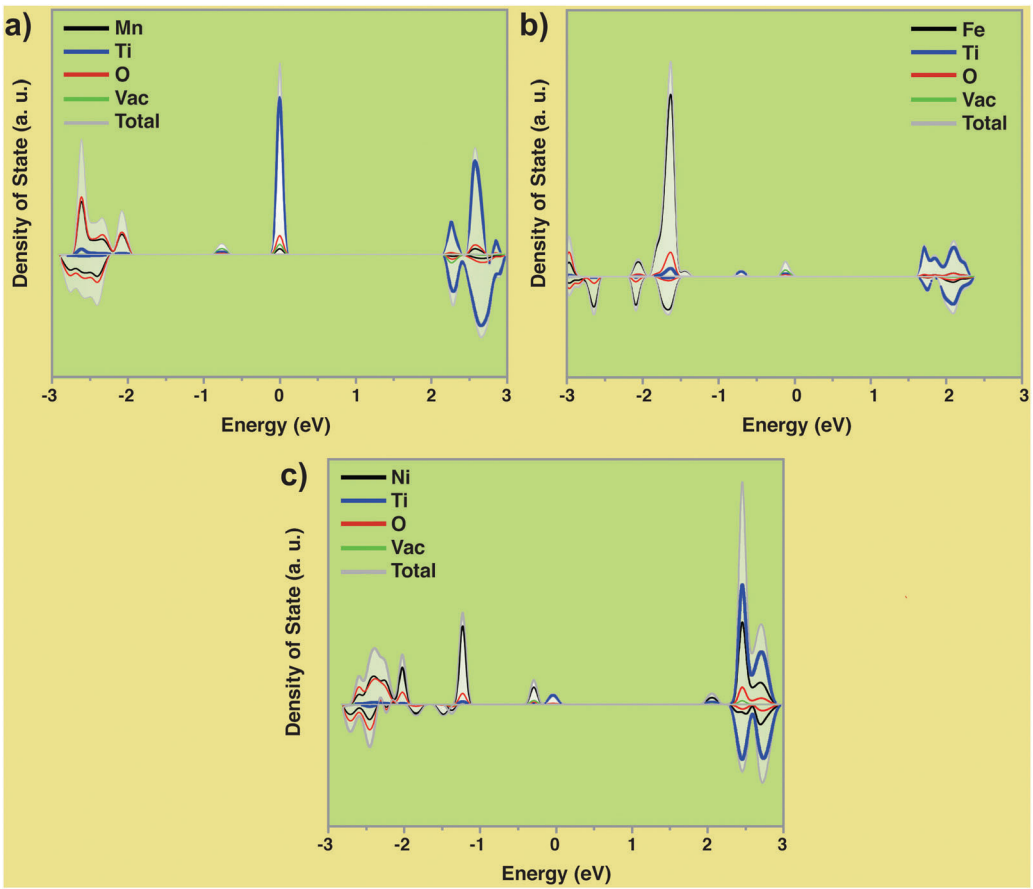

Fig. 5 Atom-resolved dos for defective (a) $MnTiO_3$, (b) $FeTiO_3$ and (c) $NiTiO_3$ non-polar (110) surfaces. The fermi level was set as zero in all cases.

ferromagnetic order inside the AFM matrix, contributing to their multifunctional properties.

The stabilization of such ground-states is now discussed by means of the DOS profiles depicted in Fig. 5. For comparative purposes, the electronic atom-resolved DOS for the pristine (110) surfaces can be founded in ESI† (Fig. S4). An analysis of the results indicates that in all cases the $V_O^{\times}$ center contributes to the generation of intermediary energy levels in the band gap region, thus reducing the excitation energy, as observed for the defective bulk models (Fig. 4). For both ferromagnetic $MnTiO_3$ and $FeTiO_3$ (110) surfaces (Fig. 5a and b), two non-degenerate bands were found inside the band gap region, indicating electron localization in empty 3d orbitals. For $MnTiO_3$, a huge contribution of Ti(3d) states was found in the vicinity of the Fermi level, indicating that both electrons from $V_O^{\times}$ are localized in empty 3d states generating magnetic parallel ordered $[TiO_4]'$ species. In addition, this state is well-localized crossing the Fermi level, generating half-metallic behavior for the defective $MnTiO_3$ (110) surfaces, where the material is a metal for the spin-up channel while behaving as a semiconductor for the spin-down channel. On the other hand, for $FeTiO_3$, both $V_O^{\times}$ and Ti(3d) states present similar contributions, showing that one electron remains in the $V_O^{\times}$ with parallel spin orientation and one electron remains in the Ti($3d^1$) state. In an opposite way, for $NiTiO_3$, an almost degenerate contribution of Ti(3d) and Ni(3d) states was found closer to the Fermi level, suggesting an antiparallel orientation between the remaining electrons, which are located in empty β orbitals of Ni($3d^8$) and Ti($3d^1$-α).

Aiming to represent the unpaired electron density distribution in the vicinity of the $V_O^{\times}$ in the $MnTiO_3$ and $FeTiO_3$ (110) surface planes, the magnetization density was investigated from spin density isosurfaces, as depicted in Fig. 6. An analysis of the results shows the presence of the magnetic ground state near the vacancy, confirming the spin population along the Ti atoms neighboring the vacant sites that is responsible for generating the magnetic $[TiO_5]'$ species. In particular, the Ti($3d^1$) orbitals are hybridized with the vacancy states; therefore, the AFM ground-state of the magnetic A^{2+} cations neighboring the $V_O^{\times}$ remains stable for $MnTiO_3$ and $FeTiO_3$ materials, but an overall magnetic contribution was attributed to spin-up reduced $[TiO_5]'$ clusters, resulting in local ferromagnetic ordering which is suitable for superior multiferroic applications and spintronic technologies.

These results confirm that tuning $V_O^{\times}$ can effectively change the structural, magnetic, and electronic degrees of freedom in $ATiO_3$ (A = Mn, Fe, Ni). It should be emphasized that the manipulation of magnetism is achieved through the medium of the Ti sites, revealing superior multiferroic properties, mainly for $MnTiO_3$ and $FeTiO_3$, which exhibit local ferromagnetic ordering.

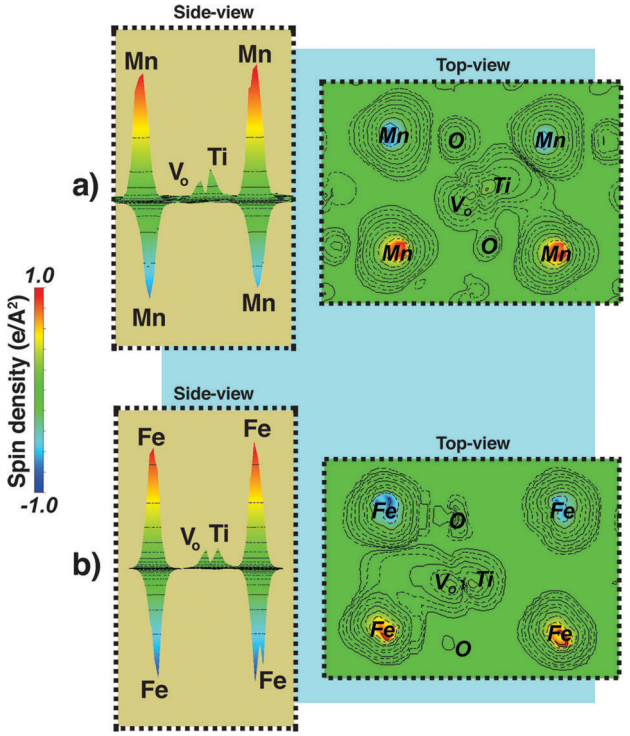

Fig. 6 Spin density distribution closer to the oxygen vacancy site showing ferromagnetic ordering for (a) $MnTiO_3$ and (b) $FeTiO_3$ non-polar (110) surfaces. In both cases the surface isovalue is 0.01 electron $bohr^{-3}$.

4. Conclusions

The energetics, structural, magnetic, and electronic properties of intrinsic neutral oxygen vacancies in multiferroic $ATiO_3$ (A = Mn, Ti, Fe) materials were investigated utilizing hybrid DFT calculations for both bulk and non-polar (110) surfaces. The introduction of these defects contributes to the generation of local structural and electronic disorders characterized by the existence of both $[AO_5]$ and $[TiO_5]$ clusters in the bulk, as well as undercoordinated metal cations along the (110) surface plane. These disorders combined to create intermediary energy levels which decreased the band gap energy for all materials. Magnetic measurements point out that a local ferromagnetic arrangement closer to the vacancy is lower in energy for $MnTiO_3$ and $FeTiO_3$, while $NiTiO_3$ remains antiferromagnetic for both bulk and surface models. The emergence of ferromagnetism for $MnTiO_3$ and $FeTiO_3$ is the result of oxygen vacancy-created $[TiO_5]'(3d^1)$ defect states, which mediate the ferromagnetic coupling between the localized A^{2+} spins in the bulk. For the (110) surface, the ferromagnetic order was attributed to the $[TiO_4]'(3d^1)$ species that lie exposed along the surface plane increasing the local magnetic moment, resulting in the particular half-metallic behavior of $MnTiO_3$. Finally, a mechanism is proposed for controlling multiple order parameters of $ATiO_3$ materials simultaneously by using a single parameter, $V_O^{\times}$, suggesting superior multiferroic orders, which make these materials suitable for multifunctional device applications.

Conflicts of interest

There are no conflicts to declare.

Acknowledgements

This work was supported by the State University of Ponta Grossa, University of Jaume I, CAPES, PDSE-CAPES and FundaçãoAraucária. J. A. acknowledges the financial support of the following agencies: Generalitat Valenciana for PrometeoII/2014/022, Prometeo/2016/079, ACOMP/2014/270, ACOMP/2015/1202, Ministerio de Economia y Competitividad, project CTQ2015-65207-P. E. Longo acknowledges the financial support of FAPESP 2013/07296-2. The authors thanks to Enio Longo for the support with the scientific illustrations.

References

1 S.-W. Cheong and M. Mostovoy, *Nat. Mater.*, 2007, **6**, 13.
2 D. I. Khomskii, *J. Magn. Magn. Mater.*, 2006, **306**, 1–8.
3 M. M. Vopson, *Crit. Rev. Solid State Mater. Sci.*, 2015, **40**, 223–250.
4 N. A. Benedek and C. J. Fennie, *J. Phys. Chem. C*, 2013, **117**, 13339–13349.
5 E. Claude and J. F. Craig, *J. Phys.: Condens. Matter*, 2008, **20**, 434219.
6 V. E. Dmitrienko, E. N. Ovchinnikova, S. P. Collins, G. Nisbet, G. Beutier, Y. O. Kvashnin, V. V. Mazurenko, A. I. Lichtenstein and M. I. Katsnelson, *Nat. Phys.*, 2014, **10**, 202.
7 T. Varga, A. Kumar, E. Vlahos, S. Denev, M. Park, S. Hong, T. Sanehira, Y. Wang, C. J. Fennie, S. K. Streiffer, X. Ke, P. Schiffer, V. Gopalan and J. F. Mitchell, *Phys. Rev. Lett.*, 2009, **103**, 047601.
8 A. M. Arévalo-López and J. P. Attfield, *Phys. Rev. B: Condens. Matter Mater. Phys.*, 2013, **88**, 104416.
9 C. J. Fennie, *Phys. Rev. Lett.*, 2008, **100**, 167203.
10 X. Hao, Y. Xu, C. Franchini and F. Gao, *Phys. Status Solidi B*, 2015, **252**, 626–634.
11 N. Mufti, G. R. Blake, M. Mostovoy, S. Riyadi, A. A. Nugroho and T. T. M. Palstra, *Phys. Rev. B: Condens. Matter Mater. Phys.*, 2011, **83**, 104416.
12 T. Varga, T. C. Droubay, M. E. Bowden, R. J. Colby, S. Manandhar, V. Shutthanandan, D. Hu, B. C. Kabius, E. Apra, W. A. Shelton and S. A. Chambers, *J. Vac. Sci. Technol., B: Nanotechnol. Microelectron.: Mater., Process., Meas., Phenom.*, 2013, **31**, 030603.
13 T. Varga, T. C. Droubay, L. Kovarik, M. I. Nandasiri, V. Shutthanandan, D. Hu, B. Kim, S. Jeon, S. Hong, Y. Li and S. A. Chambers, *ACS Appl. Mater. Interfaces*, 2017, **9**, 21879–21890.
14 T. Varga, A. Kumar, E. Vlahos, S. Denev, M. Park, S. Hong, T. Sanehira, Y. Wang, C. J. Fennie, S. K. Streiffer, X. Ke, P. Schiffer, V. Gopalan and J. F. Mitchell, *Phys. Rev. Lett.*, 2009, **103**, 047601.
15 C. Xin, Y. Wang, Y. Sui, Y. Wang, X. Wang, K. Zhao, Z. Liu, B. Li and X. Liu, *J. Alloys Compd.*, 2014, **613**, 401–406.

16 R. A. P. Ribeiro, A. Camilo and S. R. de Lazaro, *J. Magn. Magn. Mater.*, 2015, **394**, 463–469.
17 R. A. P. Ribeiro and S. R. de Lazaro, *RSC Adv.*, 2014, **4**, 59839–59846.
18 R. A. P. Ribeiro, S. R. de Lazaro and C. Gatti, *RSC Adv.*, 2016, **6**, 101216–101225.
19 R. J. Tilley, in *Defects in Solids*, ed. R. J. Tilley, John Wiley and Sons, Hoboken, 2008, DOI: 10.1002/9780470380758.ch1.
20 E. Albanese, C. Di Valentin and G. Pacchioni, *ACS Appl. Mater. Interfaces*, 2017, **9**, 23212–23221.
21 H. Choi, J. D. Song, K. R. Lee and S. Kim, *Inorg. Chem.*, 2015, **54**, 3759–3765.
22 K. Inzani, T. Grande, F. Vullum-Bruer and S. M. Selbach, *J. Phys. Chem. C*, 2016, **120**, 8959–8968.
23 Y. Li, W. G. Schmidt and S. Sanna, *J. Chem. Phys.*, 2014, **89**, 234113.
24 H. A. Tahini, X. Tan, S. N. Lou, J. Scott, R. Amal, Y. H. Ng and S. C. Smith, *ACS Appl. Mater. Interfaces*, 2016, **8**, 10911–10917.
25 F. Wang, C. Di Valentin and G. Pacchioni, *Phys. Rev. B: Condens. Matter Mater. Phys.*, 2011, **84**, 0731037.
26 Y. Zhang, J. Wang, M. P. Sahoo, T. Shimada and T. Kitamura, *Phys. Chem. Chem. Phys.*, 2015, **17**, 27136–27144.
27 E. Albanese, A. Ruiz Puigdollers and G. Pacchioni, *ACS Omega*, 2018, **3**, 5301–5307.
28 A. R. Puigdollers, F. Illas and G. Pacchioni, *J. Phys. Chem. C*, 2016, **120**, 4392–4402.
29 G. Pacchioni, in *Defects at Oxide Surfaces*, ed. J. Jupille and G. Thornton, Springer International Publishing, Heidelberg, 1st edn, 2015, ch. 1, p. 462.
30 G. Pacchioni, *ChemPhysChem*, 2003, **4**, 1041–1047.
31 K. Yang, Y. Dai, B. Huang and Y. P. Feng, *Phys. Rev. B: Condens. Matter Mater. Phys.*, 2010, **81**, 033202.
32 N. A. Spaldin, S.-W. Cheong and R. Ramesh, *Phys. Today*, 2010, **63**, 38–43.
33 N. A. Hill, *J. Phys. Chem. B*, 2000, **104**, 6694–6709.
34 T. Shimada, T. Matsui, T. Xu, K. Arisue, Y. Zhang, J. Wang and T. Kitamura, *Phys. Rev. B: Condens. Matter Mater. Phys.*, 2016, **93**, 174107.
35 T. Shimada, J. Wang, Y. Araki, M. Mrovec, C. Elsässer and T. Kitamura, *Phys. Rev. Lett.*, 2015, **115**, 107202.
36 T. Xu, T. Shimada, Y. Araki, J. Wang and T. Kitamura, *Nano Lett.*, 2016, **16**, 454–458.
37 T. Shimada, T. Ueda, J. Wang and T. Kitamura, *Phys. Rev. B: Condens. Matter Mater. Phys.*, 2013, **87**, 174111.
38 A. Raeliarijaona and H. Fu, *Phys. Rev. B: Condens. Matter Mater. Phys.*, 2017, **96**, 144431.
39 W. Li, Q. He, L. Wang, H. Zeng, J. Bowlan, L. Ling, D. A. Yarotski, W. Zhang, R. Zhao, J. Dai, J. Gu, S. Shen, H. Guo, L. Pi, H. Wang, Y. Wang, I. A. Velasco-Davalos, Y. Wu, Z. Hu, B. Chen, R.-W. Li, Y. Sun, K. Jin, Y. Zhang, H.-T. Chen, S. Ju, A. Ruediger, D. Shi, A. Y. Borisevich and H. Yang, *Phys. Rev. B: Condens. Matter Mater. Phys.*, 2017, **96**, 115105.
40 W. Li, R. Zhao, L. Wang, R. Tang, Y. Zhu, J. H. Lee, H. Cao, T. Cai, H. Guo, C. Wang, L. Ling, L. Pi, K. Jin, Y. Zhang, H. Wang, Y. Wang, S. Ju and H. Yang, *Sci. Rep.*, 2013, **3**, 2618.
41 S. Deng, S. Cheng, C. Xu, B. Ge, X. Sun, R. Yu, W. Duan and J. Zhu, *ACS Appl. Mater. Interfaces*, 2017, **9**, 27322–27331.
42 S. Cheng, M. Li, S. Deng, S. Bao, P. Tang, W. Duan, J. Ma, C. Nan and J. Zhu, *Adv. Funct. Mater.*, 2016, **26**, 3589–3598.
43 J. Wang, J. B. Neaton, H. Zheng, V. Nagarajan, S. B. Ogale, B. Liu, D. Viehland, V. Vaithyanathan, D. G. Schlom, U. V. Waghmare, N. A. Spaldin, K. M. Rabe, M. Wuttig and R. Ramesh, *Science*, 2003, **299**, 1719–1722.
44 G. Catalan and J. F. Scott, *Adv. Mater.*, 2009, **21**, 2463–2485.
45 T. Rojac, A. Bencan, G. Drazic, N. Sakamoto, H. Ursic, B. Jancar, G. Tavcar, M. Makarovic, J. Walker, B. Malic and D. Damjanovic, *Nat. Mater.*, 2016, **16**, 322.
46 M. Schrade, N. Masó, A. Perejón, L. A. Pérez-Maqueda and A. R. West, *J. Mater. Chem. C*, 2017, **5**, 10077–10086.
47 J. Wu, S. Mao, Z.-G. Ye, Z. Xie and L. Zheng, *J. Mater. Chem.*, 2010, **20**, 6512–6516.
48 T. R. Paudel, S. S. Jaswal and E. Y. Tsymbal, *Phys. Rev. B: Condens. Matter Mater. Phys.*, 2012, **85**, 104409.
49 S. J. Clark and J. Robertson, *Appl. Phys. Lett.*, 2007, **90**, 132903.
50 C. Ederer and N. A. Spaldin, *Phys. Rev. B: Condens. Matter Mater. Phys.*, 2005, **71**, 224103.
51 C. Ederer and C. J. Fennie, *J. Phys.: Condens. Matter*, 2008, **20**, 434219.
52 S. Sanna and W. G. Schmidt, *Int. J. Mod. Phys. B*, 2017, **29**, 413001.
53 R. Dovesi, R. Orlando, A. Erba, C. M. Zicovich-Wilson, B. Civalleri, S. Casassa, L. Maschio, M. Ferrabone, M. De La Pierre, P. D'Arco, Y. Noël, M. Causà, M. Rérat and B. Kirtman, *Int. J. Quantum Chem.*, 2014, **114**, 1287–1317.
54 F. Corà, *Mol. Phys.*, 2005, **103**, 2483–2496.
55 M. D. Towler, N. L. Allan, N. M. Harrison, V. R. Saunders, W. C. Mackrodt and E. Aprà, *Phys. Rev. B: Condens. Matter Mater. Phys.*, 1994, **50**, 5041–5054.
56 I. de, P. R. Moreira, R. Dovesi, C. Roetti, V. R. Saunders and R. Orlando, *Phys. Rev. B: Condens. Matter Mater. Phys.*, 2000, **62**, 7816–7823.
57 C. Adamo and V. Barone, *J. Chem. Phys.*, 1999, **110**, 6158–6170.
58 R. Dovesi, A. Erba, R. Orlando, C. M. Zicovich-Wilson, B. Civalleri, L. Maschio, M. Rérat, S. Casassa, J. Baima, S. Salustro and B. Kirtman, *Wiley Interdiscip. Rev.: Comput. Mol. Sci.*, 2018, e1360.
59 R. A. P. Ribeiro, J. Andrés, E. Longo and S. R. Lazaro, *Appl. Surf. Sci.*, 2018, **452**, 463–472.
60 H. J. Monkhorst and J. D. Pack, *Phys. Rev. B: Condens. Matter Mater. Phys.*, 1976, **13**, 5188–5192.
61 T. S. Bjorheim, M. Arrigoni, D. Gryaznov, E. Kotomin and J. Maier, *Phys. Chem. Chem. Phys.*, 2015, **17**, 20765–20774.
62 F. A. Kröger and H. J. Vink, in *Solid State Physics*, ed. F. Seitz and D. Turnbull, Academic Press, 1956, vol. 3, pp. 307–435.
63 C. W. Raubach, Y. V. B. De Santana, M. M. Ferrer, P. G. C. Buzolin, J. R. Sambrano and E. Longo, *Dalton Trans.*, 2013, **42**, 11111–11116.
64 R. Uarth Fassbender, T. Strelow Lilge, S. Cava, J. Andres, L. Fernando da Silva, V. Roberto Mastelaro, E. Longo and

M. Lucio Moreira, *Phys. Chem. Chem. Phys.*, 2015, **17**, 11341–11349.

65 E. Longo, E. Orhan, F. M. Pontes, C. D. Pinheiro, E. R. Leite, J. A. Varela, P. S. Pizani, T. M. Boschi, F. Lanciotti, A. Beltrán and J. Andrés, *Phys. Rev. B: Condens. Matter Mater. Phys.*, 2004, **69**, 125115.

66 M. M. Nakata, T. M. Mazzo, G. P. Casali, F. A. La Porta and E. Longo, *Chem. Phys. Lett.*, 2015, **622**, 9–14.

67 S. Zhou, E. Čižmár, K. Potzger, M. Krause, G. Talut, M. Helm, J. Fassbender, S. A. Zvyagin, J. Wosnitza and H. Schmidt, *Phys. Rev. B: Condens. Matter Mater. Phys.*, 2009, **79**, 113201.

68 C. Di Valentin, G. Pacchioni and A. Selloni, *J. Phys. Chem. C*, 2009, **113**, 20543–20552.

69 J. B. Goodenough, *Magnetism and the chemical bond*, Interscience Publishers, 1963.

